Quantifying Thermal Infra-Red directional anisotropy using Master and Landsat-8 simultaneous acquisitions

Julien Michel, Olivier Hagolle, Simon J Hook, Jean-Louis Roujean, Philippe Gamet

Highlights

Quantifying Thermal Infra-Red directional anisotropy using Master and Landsat-8 simultaneous acquisitions

Julien Michel, Olivier Hagolle, Simon J. Hook, Jean-Louis Roujean, Philippe Gamet

- Comparing Landsat-8 and Master Surface Brightness Temperature from simultaneous acquisitions show evidences of Thermal Infra-Red directional anisotropy of up to 6K,
- Four parametric models from the litterature are fitted to the directional anisotropy effect, allowing to be reduced by up to 5.8K,
- Global models fitted on all simultaneous observations at once can still reduce directional anisotropy by up to 4.7K, reducing the error below 2K in most cases.

Quantifying Thermal Infra-Red directional anisotropy using Master and Landsat-8 simultaneous acquisitions

Julien Michel[a,*], Olivier Hagolle[a], Simon J. Hook[b], Jean-Louis Roujean[a], Philippe Gamet[a]

[a] *CESBIO, Université de Toulouse, CNES, CNRS, INRAE, IRD, UT3, 18 avenue Edouard Belin, BPI 2801, TOULOUSE Cedex 9, 31401, France*
[b] *Jet Propulsion Laboratory, California Institute of Technology, 4800 Oak Grove Drive, Pasadena, CA 91109, United States*

Abstract

Satellite observations in the Thermal Infra-Red (TIR) domain provide valuable information on Land Surface Temperatures, Evapo-Transpiration and water use efficiency useful for monitoring vegetation health, agricultural practices and urban planning. By 2030, there will be 3 new high-resolution global coverage satellite TIR missions in space, all of them with fields of view larger than ± 30°. Directional anisotropy in TIR can affect the estimation of key application variables, such as temperature, and are typically studied with field campaigns or physical modelling. In this work, we have evaluated directional effects using simultaneous measurements from Landsat-8 and the ± 45° field of view MASTER airborne TIR sensor from NASA. Differences, as high as 6K observed in the surface temperatures derived from these simultaneous observations are attributed to directional effects, with the greatest differences associated with hotspot conditions, where the solar and satellite viewing directions align. Four well studied parametric directional models were fitted to the temperature differences allowing the amplitude of the measured directional effects to be reduced to below 1K, with small variations between models. The results suggest it should be possible to implement a correction for directional effects as part of the ground segment processing for the upcoming missions.

Keywords: Thermal Infra-Red, Land Surface Temperature, MASTER, Landsat-8, Calibration, Anisotropy

1. Introduction

Earth observation satellites measuring the radiometric signal in the Thermal InfraRed (TIR) spectrum between 8-12 um are used to derive the Land Surface Temper-

*Corresponding author
Email addresses: julien.michel@cnes.fr (Julien Michel), olivier.hagolle@cnes.fr (Olivier Hagolle), simon.j.hook@jpl.nasa.gov (Simon J. Hook), jean-louis.roujean@univ-tlse3.fr (Jean-Louis Roujean), philippe.gamet@cnes.fr (Philippe Gamet)

ature (LST), which is an Essential Climate Variable (ECV). LST is used to estimate evapo-transpiration (ET) (Price, 1982; Courault et al., 2005; Anderson et al., 2012), to detect plant water stress Boulet et al. (2015) and monitor and manage irrigation. A new generation of TIR sensors planned for launch later this decade will scan the Earth at high spatial and temporal resolutions, with a revisit of about 3 days at equator (and more at higher latitudes), a ground sampling distance close to 60 m at Nadir, and 4 or 5 TIR channels, plus some optical bands (Table 1). TRISHNA Lagouarde et al. (2018) is a joint Indo-French mission developed by, CNES and ISRO, with a nominal launch date of 2025. It will be followed by the by the Surface Biology and Geology (SBG) Cawse-Nicholson et al. (2021), a joint mission between NASA and the Italian Space Agency (ASI) and the the Land Surface Temperature Mission (LSTM) Koetz et al. (2018) from the European Space Agency later this decade.

Satellite	Agency	Launch	Resolution	Revisit	FoV
TRISHNA	CNES & ISRO	2025	57 m	3d (1 sat)	34°
SBG	NASA	2027	60 m	<8d (1 sat)	34°
LSTM	ESA	2029/31	37 m	2d (2 sat)	28°
LANDSAT 8 & 9	NASA	2013/21	100 m	8d (2 sat)	7.5°
ECOSTRESS	NASA	2018	38x69 m	irregular	28°

Table 1: Main features of high resolution TIR satellites. For those missions with two satellites (2 sat), both launch years are mentioned.

1.1. Directional anisotropy in the TIR domain from high resolution imagery

Similar to the reflective domain, TIR directional effects are induced by changes in the proportions of sunlit and shaded elements within a pixel, that depends on the respective positions of the sun and viewing directions (Gastellu-Etchegorry, 1996; Norman and Becker, 1995). When the viewing directions of the satellite and sensor coincide, all shaded parts are occluded and all sunlit parts are seen, leading to a peak of LST called the hotspot. The hotspot will be present in TRISHNA, SBG and LSTM scenes in the tropics. The occurrence of hot-spot will be quite common with these satellite-sensor systems due to overpass times being close to noon. It is worth emphasizing that TRISHNA will provide a workaround to this problem by observing the same scene with at least 3 different viewing angles within 8 days, thanks to its orbit design, by contrast SBG and LSTM have opted for constant angles. Further away from the hotspot, the proportions of sunlit and shaded areas will vary, which will generate directional effects due to inherent anisotropy properties of most ground targets (Cao et al., 2019; Duffour et al., 2016).

As all the up-coming high-resolution missions cited in table 1 will have a large field of view, with maximum viewing zenith angles reaching between 30 and 40 degrees, directional effects in TIR domain may impact the accuracy of LST retrieval and downstream products Mwangi et al. (2022). Therefore, pre-processing of the Level 2 products should benefit from a correction of such directional effects, depending on the actual error budget associated with those directional effects outside of the hotspot geometric conditions.

Directional effects in the reflective domain have been well studied (Roujean et al., 1992; Roujean, 2000; Wanner et al., 1995) and model-based corrections are routinely applied to high resolution imagery such as Landsat and Sentinel-2 Claverie et al. (2018). Current TIR HR (high-resolution) satellite imagery (resolution range 10 meter - 100 meter) is acquired by instruments with a narrow field of view (FOV), such as Landsat-8 (± 7.5°) or ASTER (± 8.5°), where directional effects do not have a significant impact on LST measurement. A noticeable exception is the ECOSTRESS mission flying on-board the International Space Station (ISS) Fisher et al. (2020), with its wide FOV (± 30°). Currently, there is no systematic correction of directional effects in the level 2 data processing of ECOSTRESS Hulley and Hook (2018).

Directional effects in TIR (Bian et al., 2020, 2023) domain were primarily investigated by means of simulations of physically-based radiative transfer codes such as 1D SCOPE Yang et al. (2021) and 3D DART Gastellu-Etchegorry et al. (2017). Detailed DART mock-ups were built for various land-cover types. Another category of models, so-called parametric models (Ermida et al., 2018; Cao et al., 2021) are considered as the only means to routinely correct for directional effects and thereby be used in the ground segments processors. They were evaluated against SCOPE and DART simulations (Cao et al., 2019; Bian et al., 2018; Pinheiro et al., 2006), or by cross-comparison between field measurementsDuffour et al. (2016) and medium resolution LEO (Low Elevation Orbit) and GEO (geostationary) satellites (Guillevic et al., 2013; Ren et al., 2014; Vinnikov et al., 2012) with a large field of view. It also noteworthy that directional effects also affect the Land Surface Emissivity (LSE) (Sobrino and Cuenca, 1999; Ermida et al., 2020).

1.2. Main contributions

Simulating directional effects is valuable to help understand the underlying physics, and to calibrate and evaluate parametric models in a controlled environment. Simulations however have a limited variability with respect to the natural landscape that will be observed by a global coverage satellite mission. Databases of situ measurements also lack sufficient diversity as they focus on a few plant species and land-cover types over selected geographic areas. Lower resolution (larger area) pixels from LEO and GEO satellites TIR images are a good complement to theoretical studies and field campaigns butut their large pixels may include different types of landscapes whereas forthcoming higher resolution TIR missions will focus on a finer scale enabling evalution of water stress within a given field.

This work aims to assess a directional error budget in preparation of up-coming high spatial resolution TIR missions by utilizing on on-orbit satellite-sensor data with high spatial resolution (Landsat 8) combined with near simultaneous observations from the MODIS/ASTER airborne simulator (MASTER) Hook et al. (2001). Evidence of directional behavior has been identified and compared to several well-established directional models from the literature.

Landsat-8 is the well-known Earth-observation satellite from the Landsat series, providing a global coverage of the globe with a 16-days revisit since 2013. Landsat-8 has a TIR sensor resolution of 100 meters, though level 1 and 2 products further interpolate LST products to 30 meters. The Landsat-8 FOV is quite narrow, as its maximum VZA is 7.5°, and LST maps will be considered as acquired under near Nadir

conditions in this study. MASTER Hook et al. (2001), is an airborne sensor jointly developed by Ames Research Center (ARC), Jet Propulsion Laboratory (JPL) and the EROS Data Center, to support algorithm development, calibration and validation for theASTER and MODIS teams. The MASTER instrument has 50 channels in the 0.4 - 13 μm range, with 10 bands in the TIR wavelength range, with a large FOV (maximum VZA of 42.5°). It has been regularly flown since 1998, providing more than 658 days of acquisition. Spatial resolution ranges from 5 meters to 50 meters depending on the aircraft altitude. While Landsat-8 can provide near Nadir observations, MASTER fully covers the spatial resolution and VZA of the up-coming high resolution TIR missions listed in table 1. Though ECOSTRESS could also be used for the purpose of this work, its FOV (28°) does not cover the full field of view of the up-coming missions. Moreover, ECOSTRESS has a very large swath, and a single Landsat-8 scene only covers a fraction of the VZAs of ECOSTRESS. MASTER being an airborne sensor, it covers the full range of VZA in a very narrow swath that fits completely into a Landsat-8 image.

The remainder of this paper is organised as follows. Section 2 presents the matching methodology, the data processing, as well as the directional models and models fitting procedure. Section 3 presents LST comparison statistics for each match, the evidences of the directional effects and the performances of directional models fitted on the data. Section 4 discusses the limitations and possible follow-up to this study, and section 5 summarizes the results and future work.

2. Materials and methods

2.1. Matching methodology

The full MASTER archive metadata was provided by JPL, and Landsat-8 collection 2 level 2 archive metadata (as of 2022.02.17) was downloaded from the Land Processes DAAC. From these data all pairs of MASTER and Landsat-8 products acquired during day-time, on the same date, with acquisition times within 10 minutes of each other, and with an overlap of respective bounding boxes no less than 50% were extracted. In order to measure the difference between acquisition times, the distance presented in equation 1 is used, as it takes into account both acquisition start and end time which are available in metadata for both sensors. It is noteworthy that this distance is null if one acquisition occurs fully within the time frame of the other.

$$\Delta_T = max(max(T_{start}^{landsat8} - T_{end}^{ecostress}, 0), max(T_{start}^{ecostress} - T_{end}^{landsat8}, 0)) \quad (1)$$

Using this search process, 52 matches were identified, for which the Landsat-8 overpass occurs during MASTER track flight. Those 52 matches correspond to 24 unique MASTER tracks since one track can correspond to more than one Landsat-8 product. Among those 52 matches, 7 MASTER tracks are missing in the archive. This leaves 35 pairs for which both Landsat-8 products and MASTER L1B (radiance at sensor) and L2 (derived LST and emissivities) products are available. Among those, there are 16 pairs for which the processing described in section 2.2 does not yield a valid difference image, because of cloud occurrences or insufficient swath final overlap. Table 2 gives the products references of all valid pairs used in this study. As shown

in figure 1, all sites are located in California or nearby. Figure 2 shows a detailed map view of valid overlapping area for each MASTER track, with the overlap of the second Landsat-8 image in blue when applicable. This map shows that most of the time (tracks 3, 4, 6, 10, 12), the second Landsat-8 does not bring additional coverage, to the noticeable exception of tracks 8 and 9.

Id	MASTER track id	Landsat L2 product id
1	2013-03-29_18:06:53	LC08_L2SP_038037_20130329_20200912_02_T1
2	2013-04-11_18:14:46	LC08_L2SP_041036_20130411_20200912_02_T1
3a	2013-05-22_18:13:09	LC08_L2SP_040036_20130522_20200913_02_T1
3b	2013-05-22_18:13:09	LC08_L2SP_040037_20130522_20200913_02_T1
4	2013-12-05_18:23:35	LC08_L2SP_043035_20131205_20200912_02_T1
5a	2014-03-31_18:11:16	LC08_L2SP_039035_20140331_20200911_02_T1
5b	2014-03-31_18:11:16	LC08_L2SP_039036_20140331_20200911_02_T1
6a	2014-04-14_18:27:14	LC08_L2SP_041036_20140414_20200911_02_T1
6b	2014-04-14_18:27:14	LC08_L2SP_041037_20140414_20200911_02_T1
7	2014-04-28_18:22:43	LC08_L2SP_043035_20140428_20200911_02_T1
8a	2014-06-06_18:25:35	LC08_L2SP_044033_20140606_20200911_02_T1
8b	2014-06-06_18:25:35	LC08_L2SP_044034_20140606_20200911_02_T1
9a	2014-10-21_18:35:15	LC08_L2SP_043034_20141021_20200910_02_T1
9b	2014-10-21_18:35:15	LC08_L2SP_043035_20141021_20200911_02_T1
10a	2015-05-28_18:13:05	LC08_L2SP_040036_20150528_20200909_02_T1
10b	2015-05-28_18:13:05	LC08_L2SP_040037_20150528_20200909_02_T1
11	2018-06-19_18:28:30	LC08_L2SP_042034_20180619_20200831_02_T1
12a	2021-03-30_18:32:40	LC08_L2SP_043033_20210330_20210409_02_T1
12b	2021-03-30_18:32:40	LC08_L2SP_043034_20210330_20210409_02_T1

Table 2: List of valid MASTER and Landsat-8 pairs

2.2. Data Processing

2.2.1. Product downloads

Landsat-8 products were downloaded from the collection 2 level 2 archive from the EarthExplorer portal[1]. MASTER L1B products, containing radiances and viewing angles, as well as L2 products, containing LST and geo-location grids, were requested on the MASTER website[2]. Landsat-8 viewing angles have been computed by using a C program publicly available on USGS website[3].

2.2.2. Target variables

Both mission outputs are LST and LSE maps. But they differ in the way they are estimated. On Landsat-8, there is a single usable TIR band (B10, 10.6 - 11.19 µm), which

[1] https://earthexplorer.usgs.gov/, consulted on 2023.03.01

[2] https://masterprojects.jpl.nasa.gov/, consulted on 2023.03.01

[3] https://www.usgs.gov/landsat-missions/solar-illumination-and-sensor-viewing-angle-coefficient-file, consulted on 2022.09.12

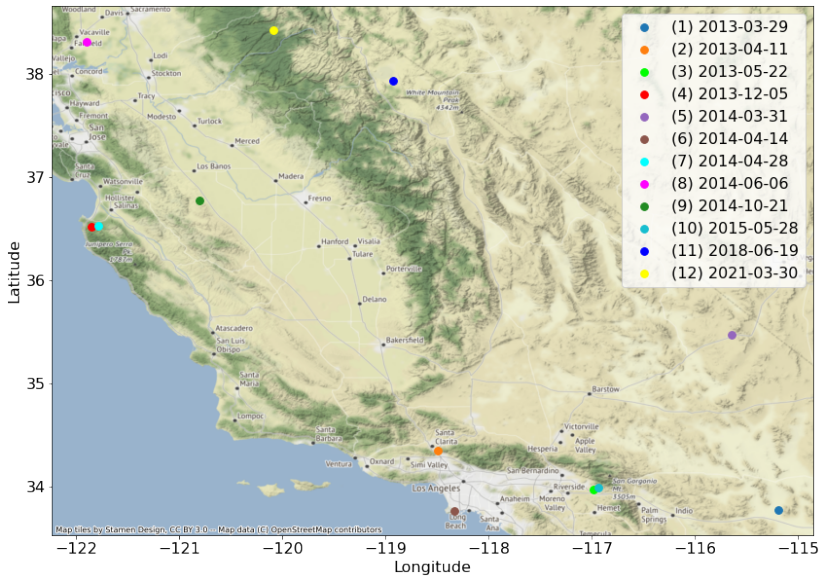

Figure 1: Location of the 12 MASTER tracks that have been matched to near simultaneous Landsat-8 acquisitions

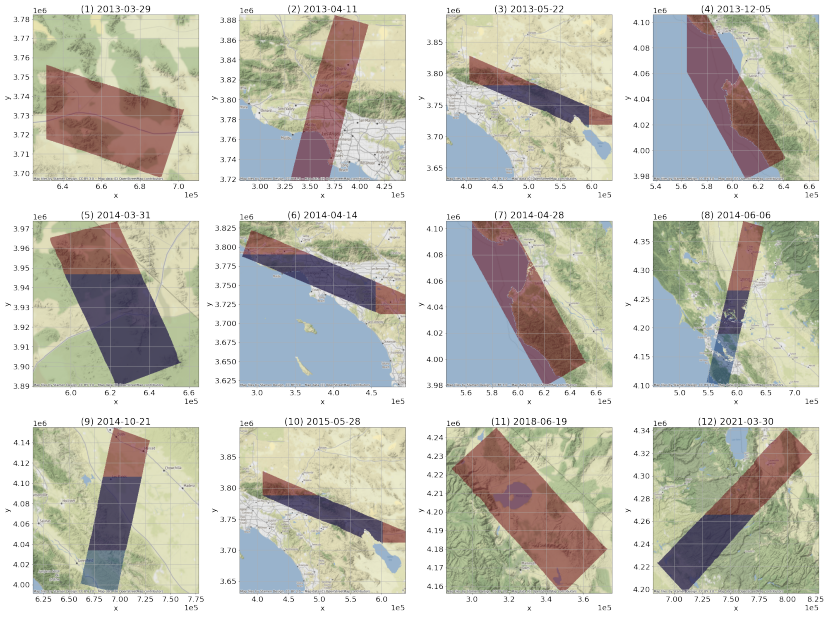

Figure 2: Detailed view of the overlapping MASTER tracks and Landsat-8 near simultaneous acquisitions. When two Landsat-8 images match a given track, the first image (a) is displayed in red and second image (b) in blue.

prevents a joint estimation of LST and LSE. LSE is therefore derived by modulating the LSE from the ASTER Global Emissivity Database Hulley et al. (2015) with the Normalized Difference Index (NDVI) and Snow Difference Index (NDSI) measured by Landsat-8. Various rules are applied to clamp emissivity values in corner cases. One important thing to note is that any emissivity lower than 0.6 is considered invalid and flagged as missing data. LST is then obtained by inverting the radiative transfer equation 2, with the atmospheric transmittance, upwelled and downwelled radiance estimated using MODTRAN, MERRA-2 and FP-IT data Malakar et al. (2018).

$$L_\lambda(\theta) = [\epsilon_\lambda B_\lambda(T_s) + (1-\epsilon_\lambda)L_\lambda^\downarrow]\tau_\lambda(\theta) + L_\lambda^\uparrow(\theta) \tag{2}$$

where $L_\lambda(\theta)$ is the at sensor radiance, λ is the wavelength, θ is the observation angle, ϵ_λ the surface emissivity, T_s is the Surface Temperature, $L_\lambda^\downarrow$ is the downwelled radiance, $\tau_\lambda(\theta)$ is the atmospheric transmittance, $L_\lambda^\uparrow(\theta)$ is the upwelled radiance and $B_\lambda(T_s)$ is the Planck function defined in equation 3.

$$B_\lambda(T_s) = \frac{2hc^2}{\pi\lambda^5\left(\exp^{\frac{hc}{k\lambda T_s}}-1\right)} = \frac{C_1}{\lambda^5\left(\exp^{\frac{C_2}{\lambda T_s}}-1\right)} \tag{3}$$

Where $h = 6.63\times10^{-34}Ws^2$ (Planck constant), $c = 2.99\times10^8 ms^{-1}$ (speed of light), $k = 1.38\times10^{-23}WsK^{-1}$ (Boltzmann constant), $C_1 = 2\pi hc^2 = 3.74\times10^{-16}Wm^2$ (first radiative constant) and $C_2 = hc/k = 1.44\times10^4\mu mK$ (second radiative constant).

MASTER, on the other hand, uses the ASTER TES algorithm to retrieve LST values Hook et al. (2011), using MODTRAN radiative transfer code and atmospheric parameters from the NCEP GDAS product. Those parameters are optimized for a flight altitude of 20 kilometers. Level 2 products include LST estimates as well emissivity estimates for channels 43, 44, 47, 48 and 49.

Since the algorithms are different for the separation of emissivity and LST, those two variables may exhibit differences that are not related to directional effects. In order to limit the impact of those differences, this study recomputes the Surface Brightness Temperature (SBT), which corresponds to the temperature of a black-body emitting the same surface radiance, for both sensors, by mean of equation 4, where $\lambda = 10.9m$ (center wavelength of Landsat-8 B10 band).

$$\text{SBT} = B_\lambda^{-1}(emis * B_\lambda(LST)) \tag{4}$$

MASTER channels 47 and 48 overlap Landsat-8 B10 spectral sensitivity response, as shown in figure 3. Since the overlaps are significant, an interpolated MASTER emissivity is derived at Landsat-8 B10 wavelength center, by means of linear interpolation of emissivities of channel 47 and 48, and will be used as the MASTER emissivity in this study.

2.2.3. Geometric processing

In order to compare measurements from products from the different sensors, they need to be first resampled to a common cartographic sampling grid. For each pair, this grid is defined using the Universal Transverse Mercator (UTM) cartographic projection

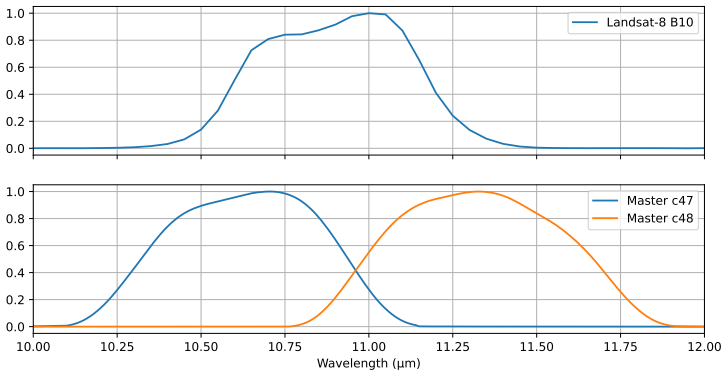

Figure 3: Spectral Sensitivity Response of Landsat-8 and MASTER overlapping Thermal Infra-Red spectral bands

of the Landsat-8 image of the pair. The sampling grid is defined according to the overlap area of the two products, and aligned to a multiple of the target resolution. The target resolution is set to 100 meter for pairs of Landsat-8 and MASTER images, since the native resolution of Landsat-8 TIR bands is 100 meters.

Landsat-8 resampling is achieved through an averaging filter, which should not incur any aliasing artifacts since the Landsat-8 LST and emissivity measurements are resampled at 30 meters resolution through bicubic interpolation. MASTER being a whisk-broom sensor, its sampling is regular in viewing angle and therefore irregular in ground geometry : both spacing between pixels and pixel size increase with the viewing angle. Resampling of those measurements to the target ground grid is achieved by means of Gaussian Weights Averaging (GWA), as described in equation 5, through its implementation in the *pyresample* library Hoese et al. (2022).

$$V(x,y) = \sum_{i \in N(x,y)} e^{\frac{-(x-x_i)^2+(x-x_i)^2}{\sigma^2}} V_i \tag{5}$$

Where (V_i, x_i, y_i) are swath samples of measurement V at location (x_i, y_i), $N(x,y)$ are the N nearest neighbours of target ground location (x,y), and σ is a user-defined parameter, which is set using equation 6, where mtf is the value of the Modulation Transfer Function (MTF) at Nyquist cut-off frequency, allowing to trade level of blur and aliasing off, r is the native sensor resolution and R is the target resolution. In this work, MTF has been set to 0.1, which yields a sigma of 68.3 meters for MASTER.

$$\sigma(r,R,mtf) = \frac{max(r,R)}{\pi} \sqrt{-2ln(mtf)} \tag{6}$$

2.2.4. Quality filtering

Only samples that are marked as clear and not flagged as water or snow in the Pixel Quality Assessment mask from the Level 2 Landsat-8 products are kept for analysis. No additional quality filtering is performed on the MASTER side.

2.2.5. Angular distance

Let (θ_0, ϕ_0) and (θ_1, ϕ_1) denote two viewing directions by their zenith angle θ and azimuth angle ϕ.The angle between those two viewing directions is given by equation 7. This distance is used in this work to measure proximity to hotspot conditions, as well as to measure distance between MASTER and Landsat-8 viewing directions.

$$D_{ang}(\theta_0, \phi_0, \theta_1, \phi_1) = \arccos(\sin(\theta_0) \times \sin(\theta_1) \times \cos(\phi_0 - \phi_1) + \cos(\theta_0) \times \cos(\theta_1))) \quad (7)$$

2.3. Directional parametric models

Four models investigated in Cao et al. (2019) have been used in this work: the Ross-Li model (Roujean et al., 1992; Wanner et al., 1995; Ren et al., 2014), the LSF-Li model FRIEDL and STRAHLER (2002), the Vinnikov model Vinnikov et al. (2012) and the RL model (Roujean, 2000; Lagouarde and Irvine, 2008). They are presented in table 3, with θ_v (resp. θ_s) denotes the view (resp. solar) zenith angle, and Δ_ϕ denotes the difference between solar and view azimuth angle. Unless stated otherwise, remaining notations and kernel expressions will be those from Cao et al. (2019). The full kernel functions are not provided here for the sake of conciseness. All models m will be expressed as stated in equation 8, with $k_0, ..., k_n$ being the free parameters of the model.

$$T(\theta_v, \theta_s, \Delta_\phi) = m(\theta_v, \theta_s, \Delta_\phi, k_0, ..., k_n) \times T_{Nadir} \quad (8)$$

For the sake of consistency with the other models, the Roujean-Lagouarde (RL) kernel has been rewritten as equation 9, with f and f_n as written in paper Cao et al. (2019) (eq. 13 and 14). This mainly move the original Δ_T parameter out of the kernel formulation, in order to use it as a kernel coefficient in table 3. It must be stressed that the RL model is the only one that does not have a volumetric kernel, but only a geometric kernel. To make that more obvious, in table 3, the parameter k_0 always represents the isotropic contribution, while k_1 stands for the coefficient of the volumetric kernel (and therefore the RL model has no k_1 parameter), and k_2 is the coefficient of the geometric or hotspot kernel. The hotspot width parameter inside the exponential in 9 is labelled k_{hs}, and it should be noted that the RL model is the only model with parameters non-linearity.

$$K_{RL}(\theta_v, \theta_s, k_{hs}) = \frac{e^{-k_{hs}f} - e^{-k_{hs}f_n}}{1 - e^{-k_{hs}f_n}} \quad (9)$$

Model	Iso	Volumetric	Geometric / Hotpsot
Ross-Li	k_0	$+ k_1 K_{RossThick}(\theta_v, \theta_s, \Delta_{phi})$	$+k_2 K_{LiSparseR}(\theta_v, \theta_s, \Delta_{phi})$
LSF-Li	k_0	$+ k_1 K_{lsf}(\theta_v, \theta_s, \Delta_{phi})$	$+k_2 K_{LiDenseR}(\theta_v, \theta_s, \Delta_{phi})$
Vinnikov	k_0	$+ k_1 K_{emis}(\theta_v, \theta_s, \Delta_{phi})$	$+k_2 K_{solar}(\theta_v, \theta_s, \Delta_{phi})$
RL	k_0		$+ k_2 K_{RL}(\theta_v, \theta_s, \Delta_{phi}, k_{hs})$

Table 3: Formulations of the four directional models from Li et al. (2021) investigated in this work

$$\min_{(k_0,k_1,k_2,k_{hs})} \| m(\theta_v, \theta_s, \Delta_{phi}, k_0, ..., k_{hs}) \times T_{Nadir} - T_{Dir}(\theta_v, \theta_s, \Delta_\phi) \|^2 \quad (10)$$

In this work, the fitting of the models parameters on the data has been performed by ordinary Least-Square as stated in equation 10, where Landsat-8 SBT is used as T_{Nadir} and MASTER SBT is used as T_{Dir}. Parameters k_0, k_2 and k_{hs} are assumed to be strictly positive, and in Cao et al. (2019) the authors observe that k_1 is always negative. Additionally, k_{hs} can not equal 0 in order to avoid a null denominator in the exponential fraction. In order to enforce those constraints, while still using unconstrained least-squares fitting,the models have been re-parametrized with exponential, and a small offset of 1e-6 has been added to k_{hs} to avoid the under-determination around 0, as shown in equation 11. Optimization has been performed using the Levenberg-Marquardt algorithm implemented in scipy Virtanen et al. (2020). Initial values have been set to 1. for k_0, 0.01 for k_1 and k_2, which corresponds to a variation of Surface Brightness Temperature of 1% that is consistent with the observations in the dataset, and 1 for k_{hs}.

$$k_0 = e^{k'_0}, \quad k_1 = -e^{k'_1}, \quad k_2 = e^{k'_2}, \quad k_{hs} = 1e-6 + e^{k'_{hs}} \tag{11}$$

3. Results

3.1. Statistics per site

Table 4 shows the bias and RMSE of LST and SBT differences, for each MASTER track, and for samples for which angles between viewing directions are below 7°. Though each track exhibits an absolute LST bias lower than 1.8 K (1.6 K for SBT), the biases of each track vary significantly within this range. Standard deviation values on differences range from 0.7 K to up to 2.2 K for LST and 0.615K to 2.088K, if we exclude track (10) which exhibits a very large standard deviation. For all tracks, SBT difference standard deviation is lower than LST difference standard deviation, which makes it more suitable for the analysis in this paper, as it seems to discard discrepancies related to the different LST - emissivity separation methods. Limiting the difference in viewing angles excludes directional effects from the possible causes of this variability. Other possible explanations may include mean acquisition time difference, differences in meteorological conditions and atmospheric corrections tied to local meteorological conditions, or evolution of MASTER calibration through time. In order to concentrate the study on the directional effects, SBT differences for each track will be corrected from the bias, and therefore the standard deviation in table 4 corresponds to the Root Mean Squared Error (RMSE) of the de-biased data.

3.2. SBT Difference maps

Figure 4 shows the SBT difference maps for each track, which have been corrected from the biases shown in table 4, so that similar viewing angles between MASTER and Landsat-8 correspond to a null SBT difference on average. Most tracks exhibit a pattern related to the position in the MASTER swath, and thus to the MASTER zenith angle. This is for instance the case form tracks (2), (6), (7), (8) and (12), where MASTER SBT on the western side of the swath appears to be consistently warmer than the eastern side of the swath. Track (4) exhibits a very noisy pattern with no trends, while track (10) exhibit heavy spatial patterns unrelated to position in swath, which is consistent with the high standard deviation observed in table 4.

Track	#samples	LST Bias	LST Std dev	SBT Bias	SBT Std dev
(1) 2013-03-29	5187	-0.56	0.72	-0.978	0.687
(2) 2013-04-11	69125	0.34	1.44	0.573	1.330
(3) 2013-05-22	59011	1.39	1.64	0.992	1.494
(4) 2013-12-05	7409	0.72	1.93	0.376	1.900
(5) 2014-03-31	22037	1.22	1.02	0.780	0.610
(6) 2014-04-14	73182	0.44	1.16	0.171	1.113
(7) 2014-04-28	13012	0.59	1.03	1.008	1.081
(8) 2014-06-06	138921	-0.34	1.84	-0.074	1.758
(9) 2014-10-21	74247	-1.50	2.14	-1.601	2.088
(10) 2015-05-28	97435	-0.14	5.55	-0.271	5.441
(11) 2018-06-19	36706	-1.35	1.72	-1.627	1.642
(12) 2021-03-30	62572	-1.73	1.90	-1.081	1.703

Table 4: Bias and RMSE of Land Surface Temperature and Surface Brightness Temperature difference (Landsat-8 - MASTER) for samples with an absolute viewing angles distance bellow 7°

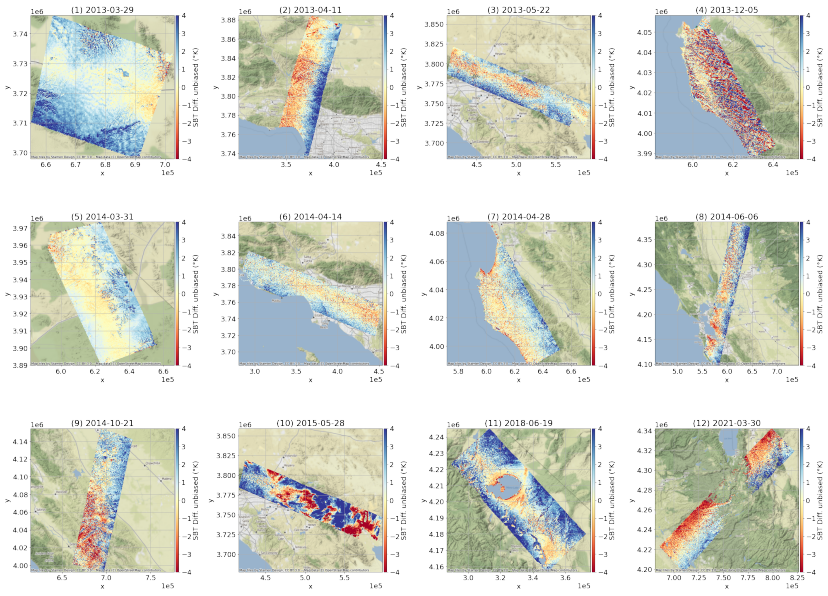

Figure 4: Maps of Surface Brightness Temperature difference (Landsat-8 - MASTER), corrected of the bias computed in table 4 for all tracks (negative values are in red and mean that MASTER is warmer than Landsat-8)

3.3. Directional effects analysis

3.3.1. Distance to hotspot vs. distance to Landsat-8 view

In figure 5, SBT differences, corrected from the biases shown in table 4, are analysed with respect to both MASTER view angular distance to hotspot and to Landsat-8 view. All graphs exhibit the same v-shaped curve, with the minimum angular distance between views occurring far from the hotspot condition (usually between 20° and 50° of distance to the hotspot). On the left of the minimum point, the MASTER view gets closer to the hotspot, which correlates with MASTER temperature getting hotter than Landsat-8 temperature. This is especially visible for tracks (2), (8) and (12), which are also the tracks that come closer to the hotspot. On the right of the minimum point, the view gets away from the hotspot condition, which correlates in most views with MASTER getting colder than Landsat-8.

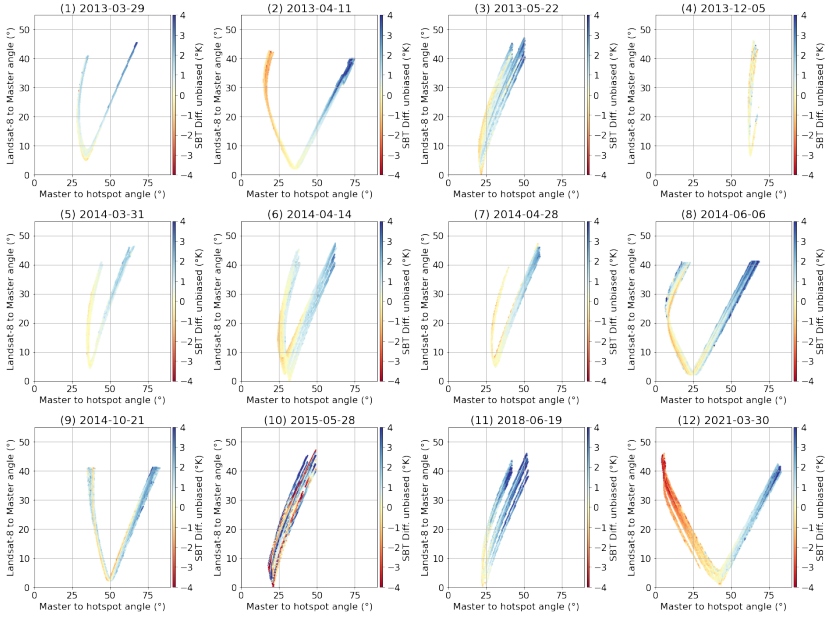

Figure 5: Surface Brightness Temperature difference (Landsat-8 - MASTER) with respect to angular distance from MASTER to hotspot and from MASTER to Landsat-8, corrected of the bias computed in table 4 (negative values are in red and mean that MASTER is warmer than Landsat-8)

3.3.2. MASTER view zenith and azimuth

Figure 6 allows better understanding the angular configurations of each MASTER track with respect to the position of the sun. Two kinds of configuration can be observed. When the sun is close to the principal observation plane, as in tracks (2), (8) and (12), the temperature steadily increases while coming closer to the sun position. On track (8), MASTER view zenith gets higher than the sun zenith which results in a cooldown of the SBT. Figure for track (10) shows that the sun is almost in the principal plane, which explain why this track has the smallest distance to the hotspot. When the

sun is far from the principal observation plane containing the solar and Nadir viewing directions, however, SBT get colder with higher view zenith angle, on both ends of the swath. The difference with Landsat-8 SBT comes to a maximum near nadir, but the position of this maximum varies and seems to be influenced by the position of the sun. This can be observed for instance for tracks (3), (5), (6), (7) and (11).

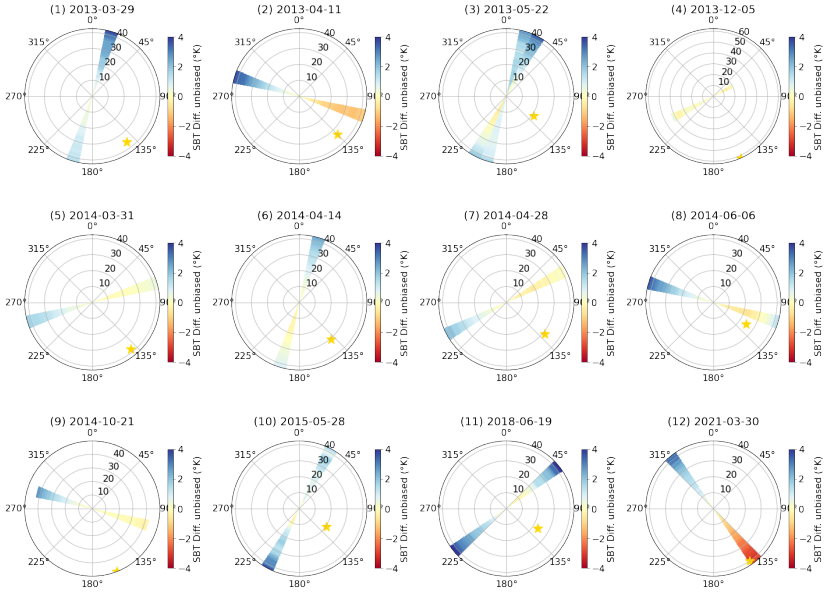

Figure 6: Surface Brightness Temperature difference (Landsat-8 - MASTER) with respect to MASTER view zenith and azimuth, corrected of the bias computed in table 4. Average sun position is marked by an orange star. (negative values are in red and mean that MASTER is warmer than Landsat-8)

Figure 7 allows better observing those two configurations. It shows the distributions of the bias-corrected SBT with respect to MASTER signed view zenith angle (positive angle are to the east and therefore closer to the sun, negative to the west). The solid red line indicates the mean difference, while the dashed red lines indicate ± 1 standard deviation. In configurations (2), (8) and (12) where the sun is almost in the principal plane, MASTER SBT gets steadily warmer than Landsat-8 from west to east. For track (8), SBT starts to get colder past the sun zenith. For tracks (3), (5), (6), (7) and (11), MASTER gets colder on both end of the swath, with a varying position for the maximum position. Dotted blue vertical lines indicate the FOV of the up-comping TRISHNA and SBG missions.

Table 5 gives a quantitative analysis of the directional effects budget for each track. Figures presented in this table have been computed to highlight the mean difference sketched by the solid red curve in figure 7. Within MASTER FOV, amplitude of directional effects range from 1.5K to more than 6K for track (12), the closest track to hotspot conditions. Restricted to the foreseen TRISHNA and SBG FOV, this budget falls to 4.71K.

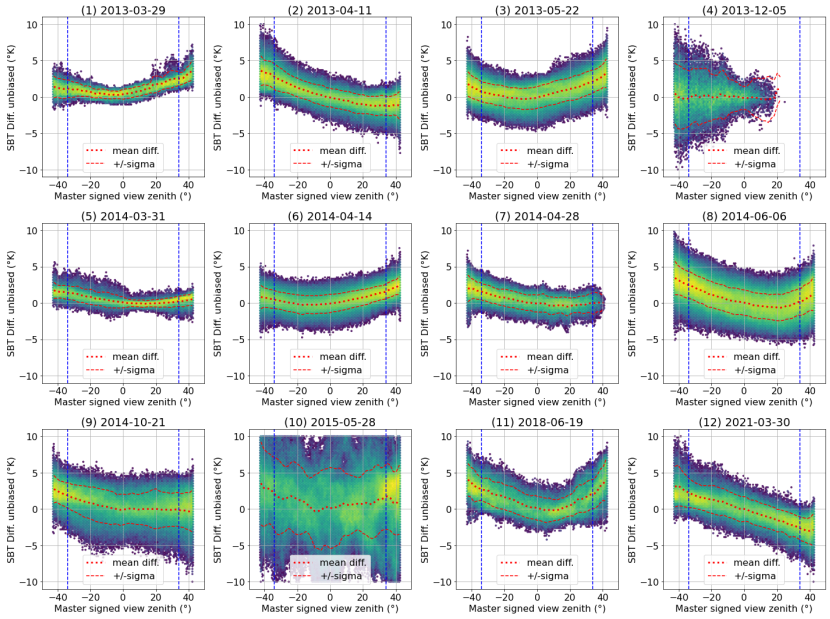

Figure 7: Surface Brightness Temperature difference, corrected of the bias computed in table 4, with respect to MASTER signed view zenith angle (positive angles are to the east, negative to the west). The solid red line indicates the mean values, the red dashed line indicates mean ± 1 standard deviation. Blue dotted lines indicate TRISHNA and SBG FOV.

	MASTER				**Trishna**			
id	Min.	-43°	43°	amp.	Min.	-34°	34°	amp.
(1)	0.25	1.38	3.66	**3.41**	0.25	1.12	2.49	**2.26**
(2)	-1.27	3.61	-1.17	**4.88**	-1.24	2.62	-1.19	**3.85**
(3)	-0.29	1.77	3.26	**3.55**	-0.29	0.64	2.03	**2.32**
(4)	-0.40	0.47	1.18	**1.57**	-0.40	-0.18	1.18	**1.57**
(5)	-0.12	1.74	0.51	**1.86**	-0.12	1.38	0.19	**1.50**
(6)	-0.27	0.81	2.40	**2.67**	-0.27	0.40	1.49	**1.75**
(7)	-0.51	2.00	0.05	**2.51**	-0.51	1.46	-0.04	**1.98**
(8)	-0.65	3.43	1.23	**4.09**	-0.65	2.43	0.13	**3.08**
(9)	-0.34	2.72	-0.30	**3.06**	-0.12	1.82	-0.04	**1.95**
(10)	-0.32	3.53	1.29	**3.85**	-0.32	1.82	1.52	**2.13**
(11)	-0.20	4.03	4.01	**4.23**	-0.20	2.64	2.03	**2.85**
(12)	-3.02	3.05	-2.87	**6.25**	-2.35	2.17	-2.54	**4.71**

Table 5: For each MASTER track, minimum average Surface Brightness Temperature difference, average Surface Brightness Temperature difference at both ends of swath and amplitude (amp.) of SBT difference between minimum and maximum are displayed, left for the master field of view, right, for a limitation to TRISHNA's field of view (all in K). The max-min column gives an estimate of directional effects.

3.4. Directional model fitting

3.4.1. Per-track parameters estimation

In this section, each of the four models presented in table 3 is fitted independently on de-biased Surface Brightness Temperature from each track, using the methodology presented in 2.3. Figure 8 shows how each model fits the scatter plot for each track, where Surface Brightness Temperature differences are expressed as a percentage variation to facilitate the comparison with the model. All models seem to be able to fit the observed directional effects, with the RL being slightly more versatile than the other, and the Vinnikov model struggling to cope with higher VZA. This can be observed for instance on tracks (2) and (12) where the Vinnikov model diverges below 0°. Hotspot shape seems to be correctly captured by the other 3 models in track (2), (8) and (12). Differences for all models start to show for higher viewing angles close to or outside limits of the data range.

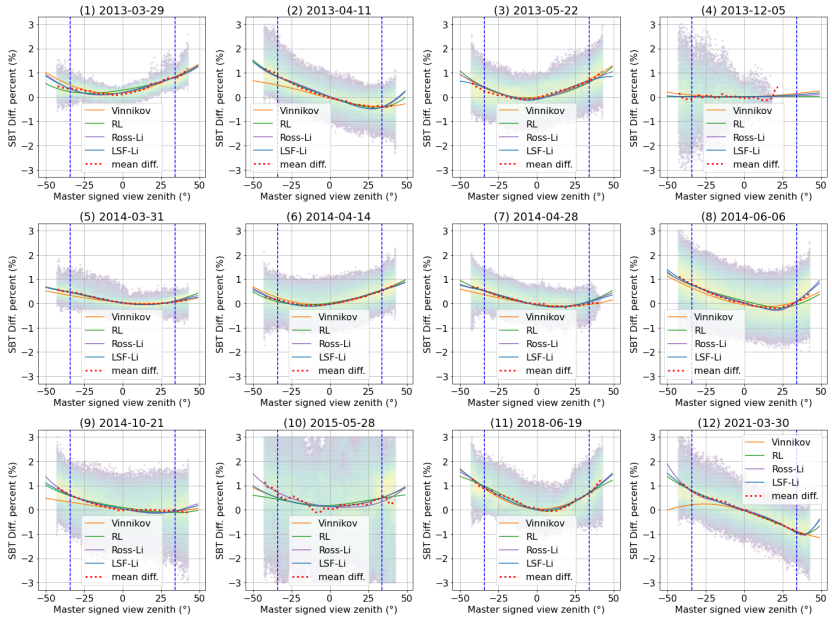

Figure 8: Least-Square fitting of the 4 TIR directional models from table 3 on Surface Brightness Temperature differences. Vertical axis represent the percentage of variation of Surface Brightness Temperature between Landsat-8 (considered as Nadir) and MASTER. In this figure, each model is fitted separately on each track.

In table 6, the correction performance of each model is measured for each track in terms of Root Mean Squared Error (RMSE) and amplitude (max - min of red curve in figure 7). Regarding RMSE, it can be observed that all models allow reducing the RMSE with respect to the uncorrected values, except for track (4) for which the correction has no effect. This can be explained by the fact that track (4) exhibits a very flat distribution shape, with no sign of directional effects (figure 7). Though performances on RMSE improvement are very close from one model to another, The Ross-Li model

is the best model for RMSE for 6 tracks, including tracks with strong hotspot such as (12) and (8). whereas the RL model only tops for 2 tracks, and the Vinnikov model for 3 tracks. Gains on RMSE range from 0.24K to 0.92K depending on the track, excluding tracks (4) and (10).

In terms of directional effects amplitude, table 6 shows that all models allow to significantly reduce the amplitude, below 1 K for the majority of tracks. Reductions for tracks with high hotspot effects are particularly strong, with track (12) going from more than 6K to less than 0.7 K for instance. The Vinnikov model is the best model for half of the tracks, but tracks with strong hotspot effect such as (8) and (12) are won by either RL or LSF-Li. Regarding amplitude, performances of the different models are less close to each other, but this can be explained by the use of maximum - minimum difference, which will be highly sensitive to outliers. Gains on directional effects amplitude range from 1.6K to 5.8K depending on the track, excluding tracks (4) and (10).

id	**RMSE**					**Amp**				
	Raw	**Vin.**	**RL**	**Ross**	**LSF**	**Raw**	**Vin.**	**RL**	**Ross**	**LSF**
(1)	1.86	**0.98**	1.02	0.99	0.98	3.41	**0.63**	1.05	1.03	0.79
(2)	2.26	1.46	**1.45**	1.49	1.48	4.88	**0.27**	0.54	1.09	1.10
(3)	2.01	**1.53**	1.56	1.55	1.55	3.55	**0.46**	0.98	1.09	1.26
(4)	3.46	3.46	3.46	3.46	3.46	1.57	1.45	1.57	1.54	1.50
(5)	1.13	0.82	**0.81**	0.82	0.81	1.86	0.37	0.44	0.30	**0.21**
(6)	1.56	1.18	1.19	**1.16**	1.16	2.67	**0.26**	0.37	0.60	0.45
(7)	1.57	**1.21**	1.22	1.21	1.21	2.51	**0.37**	0.92	0.87	0.78
(8)	2.34	1.86	1.89	**1.85**	1.85	4.09	0.79	1.25	0.72	**0.42**
(9)	2.44	2.21	2.22	**2.19**	2.21	3.06	**0.53**	0.89	1.05	0.79
(10)	4.86	4.72	4.74	**4.69**	4.72	3.85	2.63	2.83	**1.55**	2.61
(11)	2.81	1.90	1.90	**1.89**	**1.89**	4.23	1.13	1.40	**0.91**	1.05
(12)	2.65	1.85	1.85	**1.84**	1.84	6.25	0.68	**0.45**	0.65	0.50

Table 6: Root Mean-Square error and amplitude (max - min of red curve in figure 7) for raw Surface Brightness Temperature corrected of the bias computed in table 4, and for MASTER temperature normalized with four models, with parameters estimated for each track.

Figure 9 shows the raw and corrected SBT with respect to the signed VZA for 5 tracks with very strong directional effects. It can be noticed that the correction does not seem to have any effect on the standard-deviation, and thus it does not amplify or create any noise. For track (2), the best model in terms of amplitude is Vinnikov according to table 6, closely followed by RL, which can be explained by the lesser performances of the Ross-Li and LSF-Li models at higher VZA (out of TRISHNA FOV). For track (3), the best model is also Vinnikov, with amplitude two times less than the next best model, which is RL. Indeed, the latter seems to fail to completely compensate the directional trends, with SBT differences still slightly positives for positive VZA and negative for negative VZA. On track (8), the best model is LSF-Li by a large amount according to table 6, which is not that obvious on figure 9. There are remaining trends in almost all models, and all of them struggle at higher VZA. Track (11) is noisier

and the model fitting is poorer, with only the Ross-Li model achieving a correction with an amplitude below 1 K, though differences on figure 9 are not obvious. For track (12), which is the track with the strongest hotspot effect due to the proximity of MASTER viewing direction and solar direction (see figure 6), all models have strong performances according to table 6 but the RL model is the best in terms of amplitude, which is confirmed on figure 9 by fewer oscillations for higher VZA.

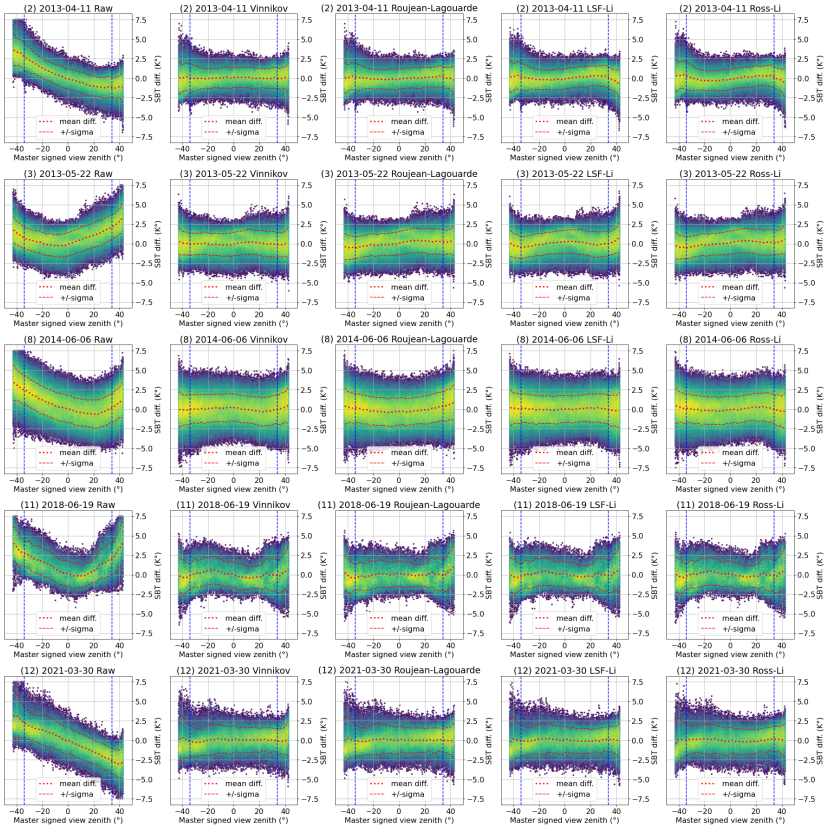

Figure 9: Corrected Surface Brightness Temperature versus signed VZA for raw and model-corrected surface brightness temperature, for 5 tracks with high directional effects amplitudes. Blue dashed lines indicate Trishna field of view.

3.4.2. Global models parameters estimation

Fitting models on each track separately allows to assess how well those models explain the observed data. However, this strategy can not apply to operational directional corrections in ground segments, where simultaneous observations will not be available to fit the models. This section investigates the performances of global models, with a single set of parameters for each model to correct all tracks at once. Parameters of those global models are fitted on all tracks altogether, using the methodology presented

in 2.3, and excluding tracks (4) and (10) for their high level of noise and lack of directional effects evidence. Figure 10 shows how well those global models with the scatter plots for each track. It can be observed that even if the goodness of fit is lesser than in figure 8, it is still relatively high, except for the Ross-Li model which seems to miss the trend of tracks (4) and (9). Global models also struggle to model the near hotspot conditions of track (12).

Table 7 shows the quantitative performance analysis of global models. As in table 6, no model clearly outperform the others. All models achieve a systematic decrease of RMSE ranging from 0.2K to 0.8K and a systematic decrease of directional effects amplitude ranging from 1.3K to 4.7K (excluding again track (4) and (10) from the analysis). Even if their performances are lower than those achieved by per track models presented in section 3.4.1, global models still provide valuable corrections.

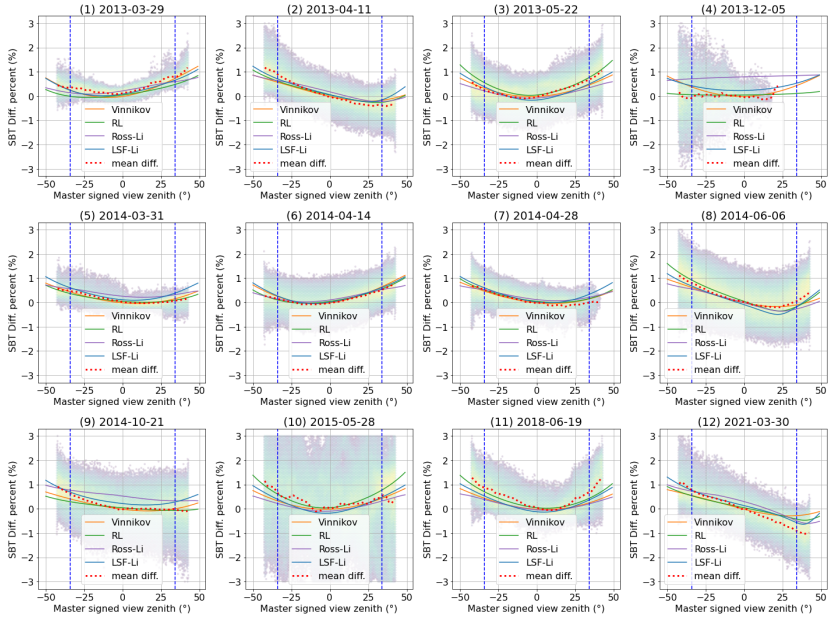

Figure 10: Least-Square fitting of the 4 TIR directional models from table 3 on Surface Brightness Temperature differences. Vertical axis represent the percentage of variation of Surface Brightness Temperature between Landsat-8 (considered as Nadir) and MASTER. In this figure, each model is jointly fitted on all tracks but (4) and (10).

Figure 11 present the same tracks as in figure 9 but corrected with the global models. While all tracks exhibit residual angular trends, within the Trishna field of view, all models exhibit performances that may be of interest for downstream applications. Track (11) has the highest residual effects, which is compliant with figures in table 7, showing a residual amplitude of around 2K for all models. On track (12), which is the closest to hotspot conditions, the Vinnikov model performs poorly with respect to the other models, and even introduces an artificial angular trend. This is again in line with the observed RMSE performance in table 7. Remaining models on track (12) all

id	RMSE					Amp				
	Raw	Vin.	RL	Ross	LSF	Raw	Vin.	RL	Ross	LSF
(1)	1.86	1.21	1.33	1.12	**1.06**	3.41	1.15	1.42	1.89	**0.99**
(2)	2.26	**1.50**	1.55	1.60	1.56	4.88	**1.02**	1.77	2.07	2.21
(3)	2.01	**1.59**	1.61	1.66	1.60	3.55	1.45	**1.09**	1.80	1.38
(4)	3.46	3.53	3.47	4.06	3.61	1.57	1.97	1.52	1.52	1.73
(5)	1.13	0.86	**0.83**	1.02	1.02	1.86	0.96	**0.54**	0.63	1.12
(6)	1.56	1.19	**1.19**	**1.19**	1.20	2.67	0.62	**0.37**	0.94	0.70
(7)	1.57	**1.23**	1.24	1.28	1.28	2.51	**0.81**	0.84	1.07	1.47
(8)	2.34	**1.88**	1.93	1.99	1.93	4.09	1.41	1.52	1.72	**0.95**
(9)	2.44	**2.22**	2.27	2.50	2.32	3.06	**0.90**	1.83	1.92	1.59
(10)	4.86	4.75	4.80	4.77	4.75	3.85	3.09	3.22	2.97	2.84
(11)	2.81	2.21	1.99	2.32	2.13	4.23	2.85	2.12	2.98	**1.94**
(12)	2.65	2.11	2.04	2.05	**1.95**	6.25	2.51	2.89	2.13	**1.57**

Table 7: Root Mean-Square error and amplitude (max - min of red curve in figure 7) for raw Surface Brightness Temperature corrected of the bias computed in table 4, and for MASTER temperature normalized with four models, with parameters jointly on all tracks except for tracks (10) and (4).

significantly reduce the angular trend that can be observed in raw SBT differences.

Figure 12 present a complete viewing angles sampling of each global model, in the mean solar conditions of track (12). All models seem to have captured the hotspot model, while the shape of the hotspot itself varies from one model to another. the Vinnikov model hotspot seem ahead of the sun zenith angle, which may explain its lesser performance in correcting track (12). Table 8 shows the estimated parameters for each model. One can note that the Ross-Li Volumetric kernel contribution is very low with respect to the others.

Model	k_0	k_1	k_2	k_{hs}
Ross-Li	1.00461367	-2.20506684e-28	0.00790642	
LSF-Li	p1.23614655	-0.22100502	0.01071329	
Vinnikov	1.00016802	-0.02243967	0.02400083	
RL	0.99956675		0.00612598	1.8459600e-08

Table 8: Parameters of the global models, estimated from all pairs but tracks (4) and (10)

4. Discussion

This study exhibit evidences of strong directional effects up to an amplitude of 6K within a FOV of ± 45°, with real high-resolution TIR data, and shows encouraging performances of state-of-the art parametric models to mitigate their impact on temperature accuracy. However, two aspects of this work need to be further analysed and discussed : the inherent limitations related to the scarce data availability on one hand, and the derivation of the model parameters in a real-world ground segment scenario.

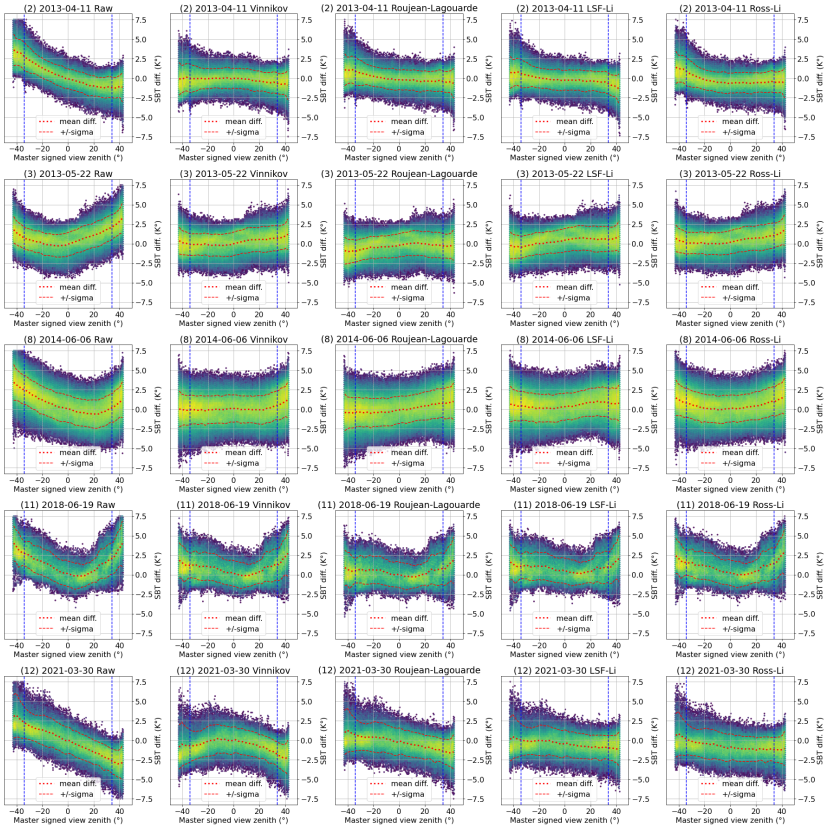

Figure 11: Corrected Surface Brightness Temperature versus signed VZA for raw and model-corrected surface brightness temperature, using models jointly fitted on all tracks but (4) and (10), for 5 tracks with high directional effects amplitudes. Blue dashed lines indicate Trishna field of view.

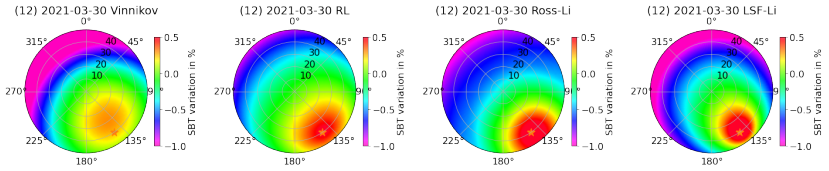

Figure 12: Polar plot of the different models, jointly fitted on all tracks but track (4) and (10), using average solar angles of track (12). Sun position is indicated by an orange star mark.

4.1. Limitations of the study

Due to the scarce availability of simultaneous observations between MASTER and Landsat-8 on one hand, and the limited coverage of MASTER flights on the other, this study only covers a limited range of landscapes, all of them located in California, U.S.. Therefore, it can not be used to draw solid conclusions on other kinds of landscape such as desert bare soil, very dense rain-forest canopy or tundras for instance. The geographic limitations also come with a low variety of solar angles conditions, excluding extreme latitude and equator for instance.

Moreover, since this study relies on Landsat-8 acquisitions which as a local over-passing time of approximately 10:30 AM, its results are mainly valid for medium morning sun angles, whereas most upcoming missions will have a local over-passing time around noon. The solar zenith angle will therefore be lower, leading to solar angular conditions that have not been analysed in this study. It is conjectured to observe lower but more frequent directional effects for sun position closer to zenith though SBT values could be higher.

Finally, this study adopts an undiscriminating point of view regarding the actual land-cover of each pixel, whereas the literature, which is driven by work on radiative transfer modeling, strongly suggests that different models or at least model parameters should be applied to different land-covers. Though we tried to determine trends related to the NDVI values from Landsat-8 in our dataset, we did not observe anything significant, and therefore the land-cover agnostic approach was privileged. However, it must be stressed that if a directional effect correction is to be implemented into up-coming missions ground-segment as a routine level 2 processing, relying on land-cover discrimination and phenology will be hard to achieve for a global coverage mission. Nevertheless, exogenous land-cover and phenology maps could be used for that purpose Phiri et al. (2020). Last, TIR directional effects in urban environment follow very different physical causes and trends (Lagouarde and Irvine, 2008; Lagouarde et al., 2010), and may require completely different models.

4.2. Model parameters estimation for up-coming ground segments

Another open question is if such a correction is to be implemented within future ground segments and which credit to give to the estimated model parameters over time, as TIR signal is ephemeral. In this study, models have been first been fitted to each track independently, resulting in good correction performances of up to 5.8K in amplitude, but with important variations of the parameters from one track to another. Such variability suggests that models parameters might depend on land unit or equivalently to target structure, and that reliability of parameters estimation depends on the observation condition they are fitted to. For instance, the RL kernel, which has been designed to model hotspot, is the best performing kernel for track (12) that is closest to hotspot condition, which can be explained either because this model is a good model for hotspot or that it requires hotspot condition to be fitted properly. It must however again be stressed that such scene based individual parameters estimation is out of reach for routinely correcting data from global coverage satellites such as TRISHNA, LSTM or SBG.

On the other hand, the global models that have been fitted simultaneously on all tracks still exhibit interesting correction performances of up to 4.7K in the studied

tracks. This work therefore suggest that such global models could be used routinely in a ground segment and be beneficial for downstream applications, with the limitations already highlighted in section 4.1.

While the determination of factors that should drive model parameters is probably best served by the physical process modelling scientific community, this paper proposes valuable dataset and methodology to assess model performances before putting them into production. Though in this work the analysed data are limited to 12 tracks in California, in the future, MASTER or other airborne TIR sensors with wide field of views might be used to acquire more of those simultaneous observations with the Landsat series, effectively building a database of the assessment and calibration of directional parametric models, should attention be paid to the simultaneous over-passing time.

5. Conclusion

In this paper, simultaneous observations in space and time between Landsat-8 and the FOV MASTER airborne TIR sensors have been leveraged to analyse potential directional effects and their error budget for up-coming High Resolution TIR missions. Twelve MASTER tracks where identified with a Landsat-8 overpass during the flight and the analysis of their Surface Brightness Temperature differences exhibits directional effects ranging from 1.6K to more than 6K within MASTER full FOV depending to the proximity to hotspot conditions. Three tracks are close to those conditions and one is almost within the principal acquisition plane, leading to the highest 6K amplitude. Four states of the art parametric models for TIR anisotropy have been selected from the literature for having been extensively tested on simulated data. Those four models have been fitted to each of the identified MASTER track, using Landsat-8 as the target Nadir Surface Brightness Temperature of reference. The corrected temperature exhibits a systematic decrease of the RMSE of 0.24K to 0.92K, and a reduction of the amplitude associated to directional effects of 1.6K to 5.8K, bringing down the directional error budget to less that 1K in almost all cases. Global models, fitted simultaneously on all valid tracks, have also been assessed, with a reduction of RMSE of 0.2K to 0.8K and a reduction of the directional effect amplitude of 1.3K to 4.7K, bringing down the directional error budget below 2K in most cases. Those results suggest that future ground segments of up-coming high-resolution missions with a FOV greater than 30° would benefit from implementing such a correction. This paper also lays grounds for a directional model in flight calibration procedure for those up-coming missions, should more airborne data be gathered during Landsat overpasses in the future.

The data used in this study have been made publicly available as an open dataset Michel et al. (2023).

References

J. C. Price, Estimation of Regional Scale Evapotranspiration Through Analysis of Satellite Thermal-infrared Data, IEEE Transactions on Geoscience and Remote

Sensing GE-20 (1982) 286–292. doi:10.1109/TGRS.1982.350445, conference Name: IEEE Transactions on Geoscience and Remote Sensing.

D. Courault, B. Seguin, A. Olioso, Review on estimation of evapotranspiration from remote sensing data: From empirical to numerical modeling approaches, Irrigation and Drainage Systems 19 (2005) 223–249. URL: https://doi.org/10.1007/s10795-005-5186-0. doi:10.1007/s10795-005-5186-0.

M. C. Anderson, R. G. Allen, A. Morse, W. P. Kustas, Use of Landsat thermal imagery in monitoring evapotranspiration and managing water resources, Remote Sensing of Environment 122 (2012) 50–65. URL: https://www.sciencedirect.com/science/article/pii/S0034425712000326. doi:10.1016/j.rse.2011.08.025.

G. Boulet, B. Mougenot, J.-P. Lhomme, P. Fanise, Z. Lili-Chabaane, A. Olioso, M. Bahir, V. Rivalland, L. Jarlan, O. Merlin, B. Coudert, S. Er-Raki, J.-P. Lagouarde, The SPARSE model for the prediction of water stress and evapotranspiration components from thermal infra-red data and its evaluation over irrigated and rainfed wheat, Hydrology and Earth System Sciences 19 (2015) 4653–4672. URL: https://hess.copernicus.org/articles/19/4653/2015/. doi:10.5194/hess-19-4653-2015, publisher: Copernicus GmbH.

J.-P. Lagouarde, B. Bhattacharya, P. Crébassol, P. Gamet, S. S. Babu, G. Boulet, X. Briottet, K. Buddhiraju, S. Cherchali, I. Dadou, G. Dedieu, M. Gouhier, O. Hagolle, M. Irvine, F. Jacob, A. Kumar, K. K. Kumar, B. Laignel, K. Mallick, C. Murthy, A. Olioso, C. Ottlé, M. R. Pandya, P. V. Raju, J.-L. Roujean, M. Sekhar, M. V. Shukla, S. K. Singh, J. Sobrino, R. Ramakrishnan, The Indian-French Trishna Mission: Earth Observation in the Thermal Infrared with High Spatio-Temporal Resolution, in: IGARSS 2018 - 2018 IEEE International Geoscience and Remote Sensing Symposium, 2018, pp. 4078–4081. doi:10.1109/IGARSS.2018.8518720, iSSN: 2153-7003.

K. Cawse-Nicholson, P. A. Townsend, D. Schimel, A. M. Assiri, P. L. Blake, M. F. Buongiorno, P. Campbell, N. Carmon, K. A. Casey, R. E. Correa-Pabón, K. M. Dahlin, H. Dashti, P. E. Dennison, H. Dierssen, A. Erickson, J. B. Fisher, R. Frouin, C. K. Gatebe, H. Gholizadeh, M. Gierach, N. F. Glenn, J. A. Goodman, D. M. Griffith, L. Guild, C. R. Hakkenberg, E. J. Hochberg, T. R. H. Holmes, C. Hu, G. Hulley, K. F. Huemmrich, R. M. Kudela, R. F. Kokaly, C. M. Lee, R. Martin, C. E. Miller, W. J. Moses, F. E. Muller-Karger, J. D. Ortiz, D. B. Otis, N. Pahlevan, T. H. Painter, R. Pavlick, B. Poulter, Y. Qi, V. J. Realmuto, D. Roberts, M. E. Schaepman, F. D. Schneider, F. M. Schwandner, S. P. Serbin, A. N. Shiklomanov, E. N. Stavros, D. R. Thompson, J. L. Torres-Perez, K. R. Turpie, M. Tzortziou, S. Ustin, Q. Yu, Y. Yusup, Q. Zhang, NASA's surface biology and geology designated observable: A perspective on surface imaging algorithms, Remote Sensing of Environment 257 (2021) 112349. URL: https://www.sciencedirect.com/science/article/pii/S0034425721000675. doi:10.1016/j.rse.2021.112349.

B. Koetz, W. Bastiaanssen, M. Berger, P. Defourney, U. Del Bello, M. Drusch, M. Drinkwater, R. Duca, V. Fernandez, D. Ghent, R. Guzinski, J. Hoogeveen, S. Hook, J.-P. Lagouarde, G. Lemoine, I. Manolis, P. Martimort, J. Masek, M. Massart, C. Notarnicola, J. Sobrino, T. Udelhoven, High Spatio- Temporal Resolution Land Surface Temperature Mission - a Copernicus Candidate Mission in Support of Agricultural Monitoring, in: IGARSS 2018 - 2018 IEEE International Geoscience and Remote Sensing Symposium, 2018, pp. 8160–8162. doi:10.1109/IGARSS.2018.8517433, iSSN: 2153-7003.

J. Gastellu-Etchegorry, Modeling radiative transfer in heterogeneous 3-d vegetation canopies, Remote Sensing of Environment 58 (1996) 131–156. URL: http://dx.doi.org/10.1016/0034-4257(95)00253-7. doi:10.1016/0034-4257(95)00253-7.

J. M. Norman, F. Becker, Terminology in thermal infrared remote sensing of natural surfaces, Agricultural and Forest Meteorology 77 (1995) 153–166. URL: http://dx.doi.org/10.1016/0168-1923(95)02259-z. doi:10.1016/0168-1923(95)02259-z.

B. Cao, Q. Liu, Y. Du, J.-L. Roujean, J.-P. Gastellu-Etchegorry, I. F. Trigo, W. Zhan, Y. Yu, J. Cheng, F. Jacob, et al., A review of earth surface thermal radiation directionality observing and modeling: Historical development, current status and perspectives, Remote Sensing of Environment 232 (2019) 111304.

C. Duffour, J.-P. Lagouarde, A. Olioso, J. Demarty, J.-L. Roujean, Driving factors of the directional variability of thermal infrared signal in temperate regions, Remote Sensing of Environment 177 (2016) 248–264.

S. Mwangi, G. Boulet, A. Olioso, Assessment of an extended sparse model for estimating evapotranspiration from directional thermal infrared data, Agricultural and Forest Meteorology 317 (2022) 108882. URL: http://dx.doi.org/10.1016/j.agrformet.2022.108882. doi:10.1016/j.agrformet.2022.108882.

J.-L. Roujean, M. Leroy, P.-Y. Deschamps, A bidirectional reflectance model of the earth's surface for the correction of remote sensing data, Journal of Geophysical Research 97 (1992) 20455. URL: http://dx.doi.org/10.1029/92jd01411. doi:10.1029/92jd01411.

J.-L. Roujean, A parametric hot spot model for optical remote sensing applications, Remote Sensing of Environment 71 (2000) 197–206. URL: http://dx.doi.org/10.1016/s0034-4257(99)00080-2. doi:10.1016/s0034-4257(99)00080-2.

W. Wanner, X. Li, A. H. Strahler, On the derivation of kernels for kernel-driven models of bidirectional reflectance, Journal of Geophysical Research 100 (1995) 21077. URL: http://dx.doi.org/10.1029/95jd02371. doi:10.1029/95jd02371.

M. Claverie, J. Ju, J. G. Masek, J. L. Dungan, E. F. Vermote, J.-C. Roger, S. V. Skakun, C. Justice, The harmonized landsat and sentinel-2 surface reflectance data set, Remote Sensing of Environment 219 (2018) 145 – 161. doi:https://doi.org/10.1016/j.rse.2018.09.002.

J. B. Fisher, B. Lee, A. J. Purdy, G. H. Halverson, M. B. Dohlen, K. Cawse-Nicholson, A. Wang, R. G. Anderson, B. Aragon, M. A. Arain, et al., Ecostress: Nasa's next generation mission to measure evapotranspiration from the international space station, Water Resources Research 56 (2020) e2019WR026058.

G. Hulley, S. Hook, Ecostress level-2 lst and emissivity algorithm theoretical basis document (atbd)(no. jpl d-94643), Jet Propulsion Laboratory, California Institute of Technology (2018).

Z. Bian, J.-L. Roujean, J.-P. Lagouarde, B. Cao, H. Li, Y. Du, Q. Liu, Q. Xiao, Q. Liu, A semi-empirical approach for modeling the vegetation thermal infrared directional anisotropy of canopies based on using vegetation indices, ISPRS Journal of Photogrammetry and Remote Sensing 160 (2020) 136–148. URL: http://dx.doi.org/10.1016/j.isprsjprs.2019.12.004. doi:10.1016/j.isprsjprs.2019.12.004.

Z. Bian, J. Roujean, T. Fan, Y. Dong, T. Hu, B. Cao, H. Li, Y. Du, Q. Xiao, Q. Liu, An angular normalization method for temperature vegetation dryness index (tvdi) in monitoring agricultural drought, Remote Sensing of Environment 284 (2023) 113330. URL: http://dx.doi.org/10.1016/j.rse.2022.113330. doi:10.1016/j.rse.2022.113330.

P. Yang, E. Prikaziuk, W. Verhoef, C. van der Tol, Scope 2.0: a model to simulate vegetated land surface fluxes and satellite signals, Geoscientific Model Development 14 (2021) 4697–4712. URL: http://dx.doi.org/10.5194/gmd-14-4697-2021. doi:10.5194/gmd-14-4697-2021.

J.-P. Gastellu-Etchegorry, N. Lauret, T. Yin, L. Landier, A. Kallel, Z. Malenovsky, A. A. Bitar, J. Aval, S. Benhmida, J. Qi, G. Medjdoub, J. Guilleux, E. Chavanon, B. Cook, D. Morton, N. Chrysoulakis, Z. Mitraka, Dart: Recent advances in remote sensing data modeling with atmosphere, polarization, and chlorophyll fluorescence, IEEE Journal of Selected Topics in Applied Earth Observations and Remote Sensing 10 (2017) 2640–2649. URL: http://dx.doi.org/10.1109/jstars.2017.2685528. doi:10.1109/jstars.2017.2685528.

S. L. Ermida, I. F. Trigo, C. C. DaCamara, J.-L. Roujean, Assessing the potential of parametric models to correct directional effects on local to global remotely sensed LST, Remote Sensing of Environment 209 (2018) 410–422. URL: https://www.sciencedirect.com/science/article/pii/S0034425718300798. doi:10.1016/j.rse.2018.02.066.

B. Cao, J.-L. Roujean, J.-P. Gastellu-Etchegorry, Q. Liu, Y. Du, J.-P. Lagouarde, H. Huang, H. Li, Z. Bian, T. Hu, B. Qin, X. Ran, Q. Xiao, A general framework of kernel-driven modeling in the thermal infrared domain, Remote Sensing of Environment 252 (2021) 112157. URL: http://dx.doi.org/10.1016/j.rse.2020.112157. doi:10.1016/j.rse.2020.112157.

B. Cao, J.-P. Gastellu-Etchegorry, Y. Du, H. Li, Z. Bian, T. Hu, W. Fan, Q. Xiao, Q. Liu, Evaluation of four kernel-driven models in the thermal infrared band, IEEE Transactions on Geoscience and Remote Sensing 57 (2019) 5456–5475. URL: http://dx.doi.org/10.1109/TGRS.2019.2899600. doi:10.1109/tgrs.2019.2899600.

Z. Bian, B. Cao, H. Li, Y. Du, J.-P. Lagouarde, Q. Xiao, Q. Liu, An analytical four-component directional brightness temperature model for crop and forest canopies, Remote Sensing of Environment 209 (2018) 731–746. URL: http://dx.doi.org/10.1016/j.rse.2018.03.010. doi:10.1016/j.rse.2018.03.010.

A. Pinheiro, J. Privette, P. Guillevic, Modeling the observed angular anisotropy of land surface temperature in a savanna, IEEE Transactions on Geoscience and Remote Sensing 44 (2006) 1036–1047. URL: http://dx.doi.org/10.1109/tgrs.2005.863827. doi:10.1109/tgrs.2005.863827.

C. Duffour, J. P. Lagouarde, J. L. Roujean, A two parameter model to simulate thermal infrared directional effects for remote sensing applications, Remote Sensing of Environment 186 (2016) 250–261. URL: https://www.sciencedirect.com/science/article/pii/S0034425716303157. doi:10.1016/j.rse.2016.08.012.

P. C. Guillevic, A. Bork-Unkelbach, F. M. Gottsche, G. Hulley, J.-P. Gastellu-Etchegorry, F. S. Olesen, J. L. Privette, Directional viewing effects on satellite land surface temperature products over sparse vegetation canopies-a multisensor analysis, IEEE Geoscience and Remote Sensing Letters 10 (2013) 1464–1468. URL: http://dx.doi.org/10.1109/LGRS.2013.2260319. doi:10.1109/lgrs.2013.2260319.

H. Ren, R. Liu, G. Yan, X. Mu, Z.-L. Li, F. Nerry, Q. Liu, Angular normalization of land surface temperature and emissivity using multiangular middle and thermal infrared data, IEEE Transactions on Geoscience and Remote Sensing 52 (2014) 4913–4931. URL: http://dx.doi.org/10.1109/tgrs.2013.2285924. doi:10.1109/tgrs.2013.2285924.

K. Y. Vinnikov, Y. Yu, M. D. Goldberg, D. Tarpley, P. Romanov, I. Laszlo, M. Chen, Angular anisotropy of satellite observations of land surface temperature, Geophysical Research Letters 39 (2012) n/a–n/a. URL: http://dx.doi.org/10.1029/2012gl054059. doi:10.1029/2012gl054059.

J. A. Sobrino, J. Cuenca, Angular variation of thermal infrared emissivity for some natural surfaces from experimental measurements, Applied Optics 38 (1999) 3931. URL: http://dx.doi.org/10.1364/ao.38.003931. doi:10.1364/ao.38.003931.

S. L. Ermida, I. F. Trigo, G. Hulley, C. C. DaCamara, A multi-sensor approach to retrieve emissivity angular dependence over desert regions, Remote Sensing of Environment 237 (2020) 111559. URL: http://dx.doi.org/10.1016/j.rse.2019.111559. doi:10.1016/j.rse.2019.111559.

S. J. Hook, J. J. Myers, K. J. Thome, M. Fitzgerald, A. B. Kahle, The modis/aster airborne simulator (master)—a new instrument for earth science studies, Remote Sensing of Environment 76 (2001) 93–102.

G. C. Hulley, S. J. Hook, E. Abbott, N. Malakar, T. Islam, M. Abrams, The aster global emissivity dataset (aster ged): Mapping earth's emissivity at 100 meter spatial scale, Geophysical Research Letters 42 (2015) 7966–7976. URL: http://dx.doi.org/10.1002/2015GL065564. doi:10.1002/2015gl065564.

N. K. Malakar, G. C. Hulley, S. J. Hook, K. Laraby, M. Cook, J. R. Schott, An operational land surface temperature product for landsat thermal data: Methodology and validation, IEEE Transactions on Geoscience and Remote Sensing 56 (2018) 5717–5735. URL: http://dx.doi.org/10.1109/TGRS.2018.2824828. doi:10.1109/tgrs.2018.2824828.

S. J. Hook, et al., HyspIRI Level-2 Thermal Infrared (TIR) land surface temperature and emissivity algorithm theoretical basis document., Technical Report, Pasadena, CA: Jet Propulsion Laboratory, National Aeronautics and Space . . . , 2011.

D. Hoese, P. Lahtinen, M. Raspaud, W. Roberts, Lavergne, S. Bot, G. Holl, S. Finkensieper, G. Ghiggi, A. Dybbroe, X. Zhang, M. Itkin, A. Meraner, BENR0, A. Valentino, Nina, L. Ørum Rasmussen, lorenzo clementi, M. Valgur, D. Rykov, A. Brammer, B. Hawkins, F. Pinault, storpipfugl, owenlittlejohns, A. R. P. Morena, B. Couwenberg, B. Esse, pytroll/pyresample: Version 1.26.0 post 0, 2022. URL: https://doi.org/10.5281/zenodo.7358887. doi:10.5281/zenodo.7358887.

M. FRIEDL, A. STRAHLER, A kernel-driven model of effective directional emissivity for non-isothermal surfaces, Progress in Natural Science 8 (2002).

J.-P. Lagouarde, M. Irvine, Directional anisotropy in thermal infrared measurements over toulouse city centre during the capitoul measurement campaigns: First results, Meteorology and Atmospheric Physics 102 (2008) 173–185. URL: http://dx.doi.org/10.1007/s00703-008-0325-4. doi:10.1007/s00703-008-0325-4.

K. Li, K. Guan, C. Jiang, S. Wang, B. Peng, Y. Cai, Evaluation of four new land surface temperature (lst) products in the us corn belt: Ecostress, goes-r, landsat, and sentinel-3, IEEE Journal of Selected Topics in Applied Earth Observations and Remote Sensing 14 (2021) 9931–9945.

P. Virtanen, R. Gommers, T. E. Oliphant, M. Haberland, T. Reddy, D. Cournapeau, E. Burovski, P. Peterson, W. Weckesser, J. Bright, S. J. van der Walt, M. Brett, J. Wilson, K. J. Millman, N. Mayorov, A. R. J. Nelson, E. Jones, R. Kern, E. Larson, C. J. Carey, İ. Polat, Y. Feng, E. W. Moore, J. VanderPlas, D. Laxalde, J. Perktold, R. Cimrman, I. Henriksen, E. A. Quintero, C. R. Harris, A. M. Archibald, A. H. Ribeiro, F. Pedregosa, P. van Mulbregt, A. Vijaykumar, A. P. Bardelli, A. Rothberg, A. Hilboll, A. Kloeckner, A. Scopatz, A. Lee, A. Rokem, C. N. Woods, C. Fulton, C. Masson, C. Häggström, C. Fitzgerald, D. A. Nicholson, D. R. Hagen, D. V. Pasechnik, E. Olivetti, E. Martin, E. Wieser, F. Silva, F. Lenders, F. Wilhelm,

G. Young, G. A. Price, G.-L. Ingold, G. E. Allen, G. R. Lee, H. Audren, I. Probst, J. P. Dietrich, J. Silterra, J. T. Webber, J. Slavič, J. Nothman, J. Buchner, J. Kulick, J. L. Schönberger, J. V. de Miranda Cardoso, J. Reimer, J. Harrington, J. L. C. Rodríguez, J. Nunez-Iglesias, J. Kuczynski, K. Tritz, M. Thoma, M. Newville, M. Kümmerer, M. Bolingbroke, M. Tartre, M. Pak, N. J. Smith, N. Nowaczyk, N. Shebanov, O. Pavlyk, P. A. Brodtkorb, P. Lee, R. T. McGibbon, R. Feldbauer, S. Lewis, S. Tygier, S. Sievert, S. Vigna, S. Peterson, S. More, T. Pudlik, T. Oshima, T. J. Pingel, T. P. Robitaille, T. Spura, T. R. Jones, T. Cera, T. Leslie, T. Zito, T. Krauss, U. Upadhyay, Y. O. Halchenko, Y. Vázquez-Baeza, S. . Contributors, Scipy 1.0: Fundamental algorithms for scientific computing in python, Nature Methods 17 (2020) 261–272. URL: http://dx.doi.org/10.1038/s41592-019-0686-2. doi:10.1038/s41592-019-0686-2.

D. Phiri, M. Simwanda, S. Salekin, V. R. Nyirenda, Y. Murayama, M. Ranagalage, Sentinel-2 data for land cover/use mapping: A review, Remote Sensing 12 (2020) 2291.

J.-P. Lagouarde, A. Hénon, B. Kurz, P. Moreau, M. Irvine, J. Voogt, P. Mestayer, Modelling daytime thermal infrared directional anisotropy over toulouse city centre, Remote Sensing of Environment 114 (2010) 87–105. URL: http://dx.doi.org/10.1016/j.rse.2009.08.012. doi:10.1016/j.rse.2009.08.012.

J. Michel, O. Hagolle, S. J. Hook, J.-L. Roujean, P. Gamet, Master and Landsat-8 simultaneous acquisition datacubes for the quantification of directional anisotropy in Thermal Infra-Red domain, 2023. URL: https://doi.org/10.5281/zenodo.7757028. doi:10.5281/zenodo.7757028.